



Research article

A continuum theory for stripe-shaped magnetic domains in thin films

Stephan Wulfinghoff, Christian Dorn*

Institute of Materials Science, Kaiserstr. 2, 24143 Kiel, Germany



ARTICLE INFO

Keywords:

Domain walls
Mesoscopic theory
Finite elements
Phase-field
Closure domains

ABSTRACT

Starting from a potential-based kinematical description of continuously distributed stripe-shaped domain walls, a mesoscopic potential is derived through an averaging procedure. The resulting mesoscopic theory is formulated in terms of a few fields with physically meaningful microscopic interpretation. Based on a phenomenological closure-domain extension, a constrained energy minimization principle is introduced. A monolithic finite-element based numerical solution algorithm is proposed. Based on a consistent linearization of the numerical algorithm, quadratic convergence is obtained for the nonlinear solution procedure. A first simple examination of the theory is undertaken by simulating a thin film with spatially and temporally non-constant effective anisotropy. The results are found to be consistent with analytical predictions.

1. Introduction

Nowadays, the evolution of magnetic domains through the motion of domain walls is understood to a high degree. Experimentally, it is possible to observe a richly faceted spectrum of domain patterns and corresponding observation methods are ever developing (e.g., [1,2]). These patterns are usually explained by micromagnetic energy minimization [3]. Although the field has been extensively studied (see the textbooks by Kronmüller and Fähnle [4], Hubert and Schäfer [5] and Coey [6]), new phenomena are still discovered and unraveled (e.g., [7,8]). The Landau–Lifshitz–Gilbert equation is a well-established approach to describe micromagnetic dynamics, which has been extensively studied [9,10]. Computational micromagnetism has been successfully coupled to mechanics, enabling the simulation of micro-magnetostrictive systems (e.g., [11–13] amongst many others). Being computationally demanding, related simulations are usually restricted to system that are strongly limited in size and number of domain walls, making the investigation of mesoscale or macroscale systems virtually impossible. Although computational homogenization techniques were developed [14], the related computationally costly micro-scale problems limit their generality and applicability. In practice, one is usually either limited to microscopic systems (e.g. [15]) or phenomenological magnetic material models are chosen, often being linearized around the working point (e.g. [16]).

Continuum models on an intermediate scale – the mesoscale – are largely missing. On this scale, the number of domains is too large for economic micromagnetic simulations but the domain structure has a distinct effect on the overall system behavior. To give an

example, recent progress in magnetoelectric sensor technology uses magnetostrictive thin films being deposited on cantilevers with distinct mechanical properties and with domain wall numbers in the order of 100–1000 [17]. Further, characteristic domain wall structures occur in these thin films, often being dominated by stripe-shaped domains¹ (see Fig. 1). While the characteristic length scale of the individual domain walls is in the nm to μm -range, the sensor dimensions are in the mm-range, making micromagnetic simulations of the whole sensor virtually impossible.

This observation motivates the call for new continuum models, which are able to bridge the scale between conventional micromagnetism and phenomenological macromagnetic material models. The aforementioned models need to be tailored for and applicable to mesoscale systems which frequently occur in practice (like the stripe-shaped domains discussed above). Further, such models should enable straightforward multiphysical extensions like a coupling with a mechanical FEM-model of the thin film as well as the substrate (often a cantilever). A natural basis for such a continuum theory is to tentatively replace the individual domain walls by a continuously distributed domain wall density, the evolution equations of which should be derived from micromagnetic theory.

In the first part of this work, we propose such a theory for stripe-shaped domains in thin films, combining modeling strategies from micromagnetism, continuum dislocation theory [18–20], phase-field models [21,22] and standard-dissipative solids [23]. In the second part, a finite-element based algorithm is proposed, which uses concepts of

* Corresponding author.

E-mail addresses: swu@tf.uni-kiel.de (S. Wulfinghoff), cdo@tf.uni-kiel.de (C. Dorn).¹ The term 'stripe-shaped domains' is used to distinguish the considered domain structure from the established term 'stripe domains'. However, under certain assumptions, the present theory could most likely be extended to include stripe domains as well.

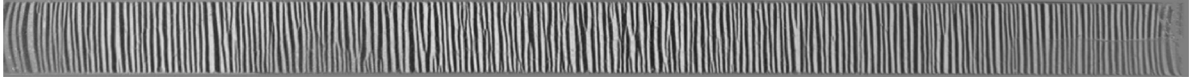


Fig. 1. Top view of the domain structure of a thin film being applied in a magnetoelectric sensor, adapted from [17] under the license CC BY 4.0 (<https://creativecommons.org/licenses/by/4.0/>).

variationally consistent updates [24,25] and algorithmically consistent tangent moduli [26].

2. Kinematics

We consider a thin-film continuum model with continuously distributed stripe shaped domain walls. The aim is to derive an ‘effective’ or ‘mesoscopic’ continuum model based on averaging a microscopic domain (wall) model being defined on a smaller scale. On the mesoscale, the thin film of thickness h is considered as a two-dimensional object. On the smaller microscale, the domain walls are considered as curved surfaces with surface normals lying within the thin-film e_1 - e_2 -plane. The thin-film surface normal coincides with the e_3 -direction.

On the mesoscale, we describe the domain wall microstructure in terms of the domain wall density $\rho(\mathbf{x}, t)$, which is interpreted as the total microscopic domain wall area per unit volume within a small/microscopic averaging (thin film) volume located at (mesoscopic) position \mathbf{x} at time t . We restrict ourselves to ‘stripe-shaped’ domains, that is, for an arbitrary control volume or area, each domain wall ‘enters’ and ‘leaves’ the control volume without intersecting with any other domain wall or forming triple junctions or the like. In that case, we can define the vector-valued domain wall density ρe_{DW}^\perp , where $e_{\text{DW}}^\perp(\mathbf{x}, t)$ denotes the local domain wall surface normal. The total number of domain walls being pierced by a mesoscopic curve C , lying in the thin-film plane, is then given by

$$\int_C \rho e_{\text{DW}}^\perp \cdot ds. \quad (1)$$

Note that the infinitesimal number of domain walls $\rho e_{\text{DW}}^\perp \cdot ds$ being pierced by the line element ds is a *signed* quantity. With the aforementioned properties of stripe-shaped domains, it follows that

$$\oint_C \rho e_{\text{DW}}^\perp \cdot ds = 0 \quad (2)$$

for an arbitrary closed curve C which, with Stokes’ theorem, implies that

$$\text{curl}(\rho e_{\text{DW}}^\perp) = \mathbf{0} \Leftrightarrow \frac{\partial(\rho e_{\text{DW}2}^\perp)}{\partial x_1} - \frac{\partial(\rho e_{\text{DW}1}^\perp)}{\partial x_2} = 0. \quad (3)$$

In other words, there is a *domain wall potential* $\gamma(x_1, x_2)$, such that

$$\rho e_{\text{DW}}^\perp = \nabla \gamma \quad (4)$$

with the property that the path-independent integral

$$\gamma(\mathbf{x}_B) - \gamma(\mathbf{x}_A) = \int_{\mathbf{x}_A}^{\mathbf{x}_B} \rho e_{\text{DW}}^\perp \cdot ds \quad (5)$$

corresponds to the effective number of domain walls being pierced by an arbitrary curve (within the thin film) connecting points A and B with position vectors \mathbf{x}_A and \mathbf{x}_B . Further, the contour lines of $\gamma(\mathbf{x})$ are parallel to the domain walls and the distance between the contour lines is proportional to the domain wall distance. This also implies that domain walls cannot start or end within the thin film, only at its boundaries.² We will see below how we can also take the influence of closure domains into account.

² In fact, a more general theory may exist, where $\text{curl}(\rho e_{\text{DW}}^\perp) \neq \mathbf{0}$. It is expected that the value of $\text{curl}(\rho e_{\text{DW}}^\perp)$ may then be related to some sort of triple junction density, which is however beyond the scope of this work.

We further describe the *microscopic* domain structure within our averaging volume by alternating ‘+’- and ‘-’-domains with corresponding alternating magnetization directions described by the in-plane unit vectors \mathbf{m}_+ and \mathbf{m}_- (i.e., neglecting the domain wall width compared to the domain width), which are also considered as mesoscopic field variables. Further, we allow for different corresponding widths d_+ and d_- as indicated in Fig. 2 and introduce the mesoscopic field variable (the *effective domain width*)

$$d_{\text{eff}} = d_+ - d_-. \quad (6)$$

For simplicity, we assume that the averaging volume is sufficiently small, such that the domain walls can be considered locally as straight. In a first approximation, one may neglect mesoscopic gradients of d_{eff} , corresponding to locally parallel domain walls in the microscopic picture (compare dashed lines in Fig. 2). However, we expect significant stray fields related to such gradients and therefore also take ∇d_{eff} into account by assuming corresponding line inclinations ω (compare full lines in the figure).

In summary, the microscopic domain structure is described on the mesoscale by the following field quantities

- domain wall potential $\gamma(\mathbf{x}, t)$ with $\nabla \gamma(\mathbf{x}, t) = \rho(\mathbf{x}, t) e_{\text{DW}}^\perp(\mathbf{x}, t)$
- effective domain width $d_{\text{eff}}(\mathbf{x}, t)$
- domain magnetization directions $\mathbf{m}_+(\mathbf{x}, t)$ and $\mathbf{m}_-(\mathbf{x}, t)$.

Below, we will additionally introduce a *closure domain phase field* $\xi(\mathbf{x}, t)$ to account for the interactions of stripe-shaped domains with closure domains.

3. Mesoscopic energy

The aim of this section is to *estimate* the mesoscopic energy as a basis for a subsequent energy/potential minimization. We assume the total energy in the averaging volume to be representable in terms of a domain wall energy E_{DW} , a stray field fluctuation energy E_φ , an anisotropy energy E_a and a Zeeman-potential E_Z :

$$E = E_{\text{DW}} + E_\varphi + E_a + E_Z. \quad (7)$$

Here, the interaction of the mesoscopic magnetization with the mesoscopic stray field is still missing but will be included below.

3.1. Domain wall energy

We assume the domain wall energy to be given by

$$E_{\text{DW}} = \int_{\Delta A_{\text{DW}}} \sigma_{\text{DW}} dA, \quad (8)$$

where σ_{DW} is the domain wall energy per unit area and ΔA_{DW} is the total domain wall area contained in the averaging volume ΔV . Assuming σ_{DW} constant, for simplicity, we find

$$E_{\text{DW}} = \sigma_{\text{DW}} \rho \Delta V = \sigma_{\text{DW}} \|\nabla \gamma\| \Delta V. \quad (9)$$

3.2. Anisotropy energy

The anisotropy energy is given by

$$E_a = \int_{\Delta V} \psi_a dV, \quad (10)$$

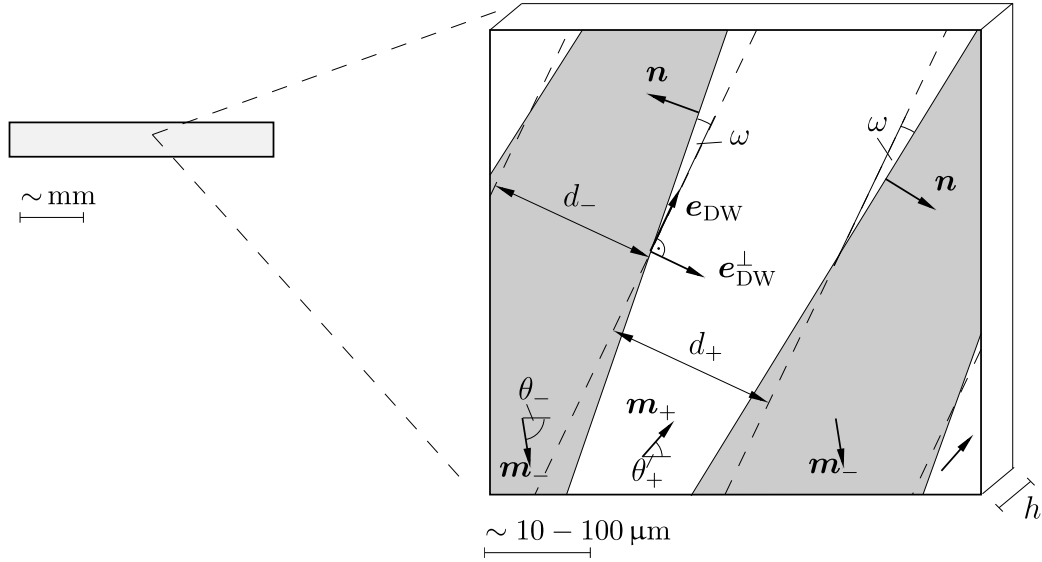


Fig. 2. Left: Two-dimensional mesoscopic thin film model (top view) with continuously distributed stripe-shaped domains. Right: Sketch of the microscopic model with resolved domains and alternating '+' and '-' domains. Note that the averaging volume should contain a sufficiently large number of domain walls. For illustration reasons it contains only four domain walls in the figure.

where ψ_a is the anisotropy energy density, depending on the microscopic magnetization. In this work, we choose for simplicity

$$\psi_a(\mathbf{m}) = K_1(1 - (\mathbf{e}_a \cdot \mathbf{m})^2) \quad (11)$$

with the anisotropy constant K_1 and the easy axis \mathbf{e}_a (a unit vector). Defining the volume fractions

$$\begin{aligned} v_+ &= \frac{d_+}{d_+ + d_-} \stackrel{(6)}{=} \frac{1}{2} \left(1 + \frac{1}{2} d_{\text{eff}} \|\nabla\gamma\| \right), \\ v_- &= \frac{d_-}{d_+ + d_-} = \frac{1}{2} \left(1 - \frac{1}{2} d_{\text{eff}} \|\nabla\gamma\| \right) \end{aligned} \quad (12)$$

and neglecting variations of \mathbf{m}_+ and \mathbf{m}_- within the averaging volume, we find

$$E_a = (v_+ \psi_a(\mathbf{m}_+) + v_- \psi_a(\mathbf{m}_-)) \Delta V. \quad (13)$$

3.3. Zeeman potential

Based on the aforementioned definitions, the mesoscopic Zeeman potential is estimated as

$$E_Z = - \int_{\Delta V} \mu_0 M^S \mathbf{m} \cdot \mathbf{H}_{\text{ext}} dV = - \mu_0 \underbrace{M^S (v_+ \mathbf{m}_+ + v_- \mathbf{m}_-)}_{\mathbf{M}} \cdot \mathbf{H}_{\text{ext}} \Delta V, \quad (14)$$

where μ_0 is the permeability of vacuum, M^S is the spontaneous magnetization, $\mathbf{M}(\mathbf{x}, t)$ is the mesoscopic magnetization and $\mathbf{H}_{\text{ext}}(\mathbf{x}, t)$ is the (slowly fluctuating) external magnetic field.

3.4. Stray field fluctuation energy

As is well-known from micromagnetic theory, magnetization jumps at the domain walls, given by

$$M^S [\mathbf{m}] \cdot \mathbf{n} = M^S (\mathbf{m}_+ - \mathbf{m}_-) \cdot \mathbf{n}, \quad (15)$$

imply magnetic surface charges. Here the domain wall normal \mathbf{n} points from '-' to '+'. The microscopic stray field fluctuations related to such surface charges are energetically costly, such that one usually can expect that $|\llbracket \mathbf{m} \rrbracket \cdot \mathbf{n}| \ll 1$. The stray field energy related to such charges is proportional to the square of the charges. In other words, we assume that there is a stray field constant k_φ such that

$$E_\varphi = k_\varphi \int_{\Delta A_{\text{DW}}} (M^S \llbracket \mathbf{m} \rrbracket \cdot \mathbf{n})^2 dA. \quad (16)$$

A longer analytical estimation (see Appendix C) yields

$$k_\varphi = D \frac{\mu_0 h}{4\pi} \quad (17)$$

with $D = 1/2 + \ln(R/h)$, where R denotes the radius of a cylindrical integration domain for the stray field calculation around a single domain wall (for details see Appendix C). For reasonable values of $R \gg h$, one obtains $D \approx 1 - 10$.

In order to make further progress, we assume the domain wall inclinations to be small, i.e., $\omega \ll 1$ (see Fig. 2). Neglecting terms in $\mathcal{O}(\omega^3)$ we can write (compare Fig. 2)

$$\omega \approx \frac{1}{4} \mathbf{e}_{\text{DW}} \cdot \nabla d_{\text{eff}}, \quad (18)$$

where \mathbf{e}_{DW} is the domain wall direction, such that $\mathbf{e}_{\text{DW}} \cdot \mathbf{e}_{\text{DW}}^\perp = 0$ and $\mathbf{e}_{\text{DW}} \cdot \mathbf{e}_3 = 0$, where \mathbf{e}_3 equals the thin-film normal direction. Consequently, the domain wall normals can be approximated by

$$\mathbf{n} \approx -\omega \mathbf{e}_{\text{DW}} \pm \underbrace{\left(1 - \frac{\omega^2}{2} \right)}_{\approx \cos \omega} \mathbf{e}_{\text{DW}}^\perp. \quad (19)$$

A straightforward computation yields

$$(\llbracket \mathbf{m} \rrbracket \cdot \mathbf{n})^2 \approx (\llbracket \mathbf{m} \rrbracket \cdot \mathbf{e}_{\text{DW}}^\perp)^2 - 2\omega^2 (\llbracket \mathbf{m} \rrbracket \cdot \mathbf{e}_{\text{DW}}^\perp)^2 + \omega^2 \|\llbracket \mathbf{m} \rrbracket\|^2 \quad (20)$$

with $\omega = \mathbf{e}_{\text{DW}} \cdot \nabla d_{\text{eff}}/4$. Assuming that, due to energetic reasons $|\llbracket \mathbf{m} \rrbracket \cdot \mathbf{n}| \ll 1$, which implies with $|\omega| \ll 1$ that $|\llbracket \mathbf{m} \rrbracket \cdot \mathbf{e}_{\text{DW}}^\perp| \ll 1$, the second term in the previous equation is small of order four and thus negligible. Thus, we find the estimate

$$E_\varphi = k_\varphi (M^S)^2 \underbrace{\|\nabla\gamma\| \Delta V}_{\Delta A_{\text{DW}}} \left((\llbracket \mathbf{m} \rrbracket \cdot \mathbf{e}_{\text{DW}}^\perp)^2 + ((\mathbf{e}_{\text{DW}} \cdot \nabla d_{\text{eff}})/4)^2 \|\llbracket \mathbf{m} \rrbracket\|^2 \right). \quad (21)$$

3.5. Further simplification of the stray field fluctuation energy

Assuming k_φ sufficiently large, E_φ will penalize any deviations of the two quantities

$$\llbracket \mathbf{m} \rrbracket \cdot \mathbf{e}_{\text{DW}}^\perp; \quad (\mathbf{e}_{\text{DW}} \cdot \nabla d_{\text{eff}}), \quad (22)$$

from zero, as long as $\|\llbracket \mathbf{m} \rrbracket\|$ takes values in the order of 1. In other words, we expect ∇d_{eff} to be almost perpendicular to the domain wall

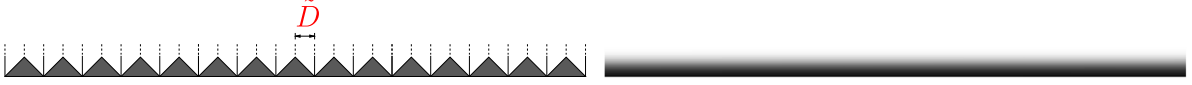


Fig. 3. Sketch of triangular closure domains (left) and their ‘smeared’ counterpart, which is the phase field (right).

direction e_{DW} and the magnetization direction jump $\llbracket \mathbf{m} \rrbracket$ to be almost perpendicular to e_{DW}^\perp , or alternatively:

$$\llbracket \llbracket \mathbf{m} \rrbracket \rrbracket e_{\text{DW}} \approx \pm \llbracket \mathbf{m} \rrbracket. \quad (23)$$

Interpreting E_φ as a penalty energy, an almost identical behavior/solution is thus expected, if one replaces Eq. (21) by the slightly more simple (computationally more attractive) expression

$$E_\varphi = k_\varphi (M^S)^2 \|\nabla \gamma\| \Delta V \left((\llbracket \mathbf{m} \rrbracket \cdot e_{\text{DW}}^\perp)^2 + ((\llbracket \mathbf{m} \rrbracket \cdot \nabla d_{\text{eff}})/4)^2 \right). \quad (24)$$

3.6. Mesoscopic energy density

Summarizing all results, we obtain the following preliminary mesoscopic potential

$$\int_A (\psi_{\text{DW}} + \psi_\varphi + \psi_A + \psi_Z + \mu_0 \mathbf{M} \cdot \nabla \varphi) dA - \int \frac{1}{2} \mu_0 \nabla \varphi \cdot \nabla \varphi dV, \quad (25)$$

where we also account in a phenomenological standard fashion for contributions from the mesoscopic stray field $-\nabla \varphi$, associated with the mesoscopic magnetization \mathbf{M} (see Eq. (14)). The potential in Eq. (25) is given in terms of the mesoscopic fields $\{\gamma, \varphi, d_{\text{eff}}, \mathbf{m}_\pm\}$ with the following mesoscopic energies

- domain wall energy density (see Eq. (9)):

$$\psi_{\text{DW}} = \sigma_{\text{DW}} \|\nabla \gamma\| \quad (26)$$

- stray field fluctuation energy density (see Eq. (16)):

$$\psi_\varphi = k_\varphi (M^S)^2 \|\nabla \gamma\| \left((\llbracket \mathbf{m} \rrbracket \cdot e_{\text{DW}}^\perp)^2 + ((\llbracket \mathbf{m} \rrbracket \cdot \nabla d_{\text{eff}})/4)^2 \right); \quad e_{\text{DW}}^\perp = \frac{\nabla \gamma}{\|\nabla \gamma\|} \quad (27)$$

- anisotropy energy (see Eq. (13)):

$$\psi_A = v_+ \psi_a(\mathbf{m}_+) + v_- \psi_a(\mathbf{m}_-); \quad v_\pm = \frac{1}{2} \left(1 \pm \frac{1}{2} d_{\text{eff}} \|\nabla \gamma\| \right), \quad (28)$$

- Zeeman potential (see Eq. (14)):

$$\psi_Z = -\mu_0 \underbrace{(v_+ \mathbf{m}_+ + v_- \mathbf{m}_-)}_{\mathbf{M}} \cdot \mathbf{H}_{\text{ext}} \quad (29)$$

4. Closure domain phase-field model

In this section, we propose a phenomenological phase-field model to account for the influence of closure domains, which are well-known to have a significant influence on both, the magnetic microstructure as well as on the stray field. We have ‘small’ closure domains in mind in the sense that the characteristic dimensions of a closure domain is significantly smaller than the in-plane dimensions of the thin film. We start by recalling a ‘standard’ phase-field energy ansatz, which is extensively used in the context of phase-field fracture models (e.g., [22]). We start with the one-dimensional theory:

$$\psi_\xi = \frac{a}{2} \left(\xi(x)^2 + (l\xi'(x))^2 \right), \quad (30)$$

where a and l are material parameters and $\xi \in [0, 1]$ is the phase-field variable, where ‘1’ means ‘closure-domain’ and ‘0’ means ‘no closure-domain’. The aim is to obtain a phase-field solution, which takes the

value 1 at the boundaries, where closure-domains are present and decay to zero with a length scale given by the characteristic closure domain dimensions. This mimics, in a diffuse sense, the triangular shape of the closure domains (see Fig. 3).

Further the phase-field energy shall properly represent the closure-domain energy. Assuming that equilibrium is characterized by an energy-minimum and considering that the phase-field quickly decays to zero, we search for solutions of the following boundary value problem

$$\delta \int_0^\infty \psi_\xi dx = 0 \quad \Leftrightarrow \quad \xi - l^2 \xi'' = 0 \quad (31)$$

with $\xi(0) = 1$ and $\xi'(\infty) = 0$. The solution and closure-domain energy per unit length read

$$\xi(x) = e^{-\frac{x}{l}}, \quad E = \int_0^\infty \psi_\xi dx = \frac{1}{2} l a. \quad (32)$$

With the aforementioned requirements

$$l = \bar{D}, \quad E = \frac{1}{2} K_1 \bar{D}, \quad (33)$$

where $\bar{D} \stackrel{!}{=} 1/\rho = 1/\|\nabla \gamma\|$ is the domain wall distance (see Fig. 3), we postulate the following thin-film (2D) phase-field energy:

$$\psi_\xi = \frac{K_1}{2} \left(\xi^2 + \left(\frac{\|\nabla \xi\|}{\|\nabla \gamma\|} \right)^2 \right). \quad (34)$$

Note that the internal length scale is not a material constant, as in most other phase-field models, but is given in terms of the domain wall distance $l = 1/\|\nabla \gamma\|$. This coupling ensures both, the geometric compatibility between the (stripe-shaped) domain fields and the phase-field as well as a proper energy exchange between the two.

5. Total potential and boundary value problem

The formulation of the total potential and the boundary value problem follows standard lines and is therefore kept short, for convenience.

5.1. Total potential

By collecting all relevant energy contributions, we are now ready to formulate the following incremental potential in terms of the mesoscopic unknown fields $\{\gamma, d_{\text{eff}}, \xi, \varphi, \mathbf{m}_\pm\}$:

$$\Pi[\gamma, d_{\text{eff}}, \xi, \varphi, \mathbf{m}_\pm] = - \int_V \frac{1}{2} \mu_0 \nabla \varphi \cdot \nabla \varphi dV \quad (35)$$

$$+ h \int_A \left(\psi_{\text{DW}} + \psi_\varphi + \psi_A + \psi_\xi + \phi_\Delta(\dot{\mathbf{m}}_+, \dot{\mathbf{m}}_-) - \mu_0 (\mathbf{H}_{\text{ext}} - \nabla \varphi) \cdot \mathbf{M} \right) dA. \quad (36)$$

Here, we added the dissipation potential ϕ_Δ to account for Gilbert-damping (see below), while precession effects are neglected. Note that the formulation here is valid for both, the time-continuous as well as the time-discrete case in the sense that $\dot{\mathbf{m}}_+$ and $\dot{\mathbf{m}}_-$ are time-discrete approximations of $\dot{\mathbf{m}}_+$ and $\dot{\mathbf{m}}_-$. In the simplest case $\dot{\mathbf{m}}_\pm = \Delta \mathbf{m}_\pm / \Delta t$, which will also be adopted in this work. The time-continuous limit is recovered for $\Delta t \rightarrow 0$.³ The volume V in general represents the Euclidean

³ In the time-continuous limit, all fields are obtained at any time by optimization of the total potential Π except for \mathbf{m}_\pm . The rates of the latter are computed by minimization of a rate-potential being the time-continuous counterpart of Π , which is defined in Appendix D.

space, but will be restricted to a finite volume for practical computational reasons. We assume that the behavior of the thin film is governed by the following optimization problem

$$\{\gamma, d_{\text{eff}}, \xi, \varphi, \mathbf{m}_{\pm}\} = \arg \inf_{\gamma \in \kappa_{\gamma}} \inf_{d_{\text{eff}}} \inf_{\xi \in \kappa_{\xi}} \inf_{\mathbf{m}_{\pm}} \sup_{\varphi \in \kappa_{\varphi}} \Pi[\gamma, d_{\text{eff}}, \xi, \varphi, \mathbf{m}_{\pm}]. \quad (37)$$

Here the κ 's are appropriate sets of functions satisfying suitable Dirichlet boundary conditions, which are further discussed below by means of example. Note that for vanishing dissipation potential, i.e. $\phi_{\Delta} = 0$, the statement (37) corresponds to an overall energy minimization requirement with the constraint that Gauss' law of magnetostatics be satisfied (through the 'sup'-condition, see below).

5.2. Boundary value problem

5.2.1. Weak form

For the variables $\{\gamma, d_{\text{eff}}, \xi\}$, the minimization conditions read

$$\delta_{\alpha} \Pi = h \int_A (\partial_{\alpha} \pi \delta \alpha + \partial_{\nabla \alpha} \pi \cdot \nabla \delta \alpha) dA \ni 0, \quad (38)$$

where $\alpha \in \{\gamma, d_{\text{eff}}, \xi\}$ and π is a short notation for the integrand in expression (36). Further, the notation ' $\ni 0$ ' accounts for the fact that π is not differentiable in all points (in particular in the case of a vanishing domain wall density), which in principle can be partially handled mathematically through subdifferentials. However, for the moment we have exclusively applications in mind which do not require the treatment of non-differentiable points. Therefore, the ' \ni ' will be replaced by '=' in the following, for simplicity.

The 'sup'-condition related to the magnetostatic potential φ reads

$$\delta_{\varphi} \Pi = h \int_A \mu_0 \mathbf{M} \cdot \nabla \delta \varphi dA - \int_V \mu_0 \nabla \varphi \cdot \nabla \delta \varphi dV = 0 \quad (39)$$

5.2.2. Strong form

By standard calculations, we obtain from the weak form discussed above the following strong form (with appropriate boundary normals \mathcal{N}):

- For $\alpha \in \{\gamma, d_{\text{eff}}, \xi\}$:

$$\partial_{\alpha} \pi - \text{div}_2(\partial_{\nabla \alpha} \pi) = 0 \text{ in } A; \quad \mathcal{N} \cdot \partial_{\nabla \alpha} \pi = 0 \text{ on } \partial A_{\mathcal{N}}, \quad (40)$$

where ' div_2 ' is the in-plane divergence and $\partial A_{\mathcal{N}}$ denotes the 'Neumann'-'Non-Dirichlet'-part of the boundary.

- For φ :

$$\Delta \varphi = 0 \text{ in } V \setminus A; \quad -\mathcal{N} \cdot \llbracket \nabla \varphi \rrbracket = -h \text{div}_2(\mathbf{M}) \text{ on } A; \quad \mathbf{M} \cdot \mathcal{N} = 0 \text{ on } \partial A \quad (41)$$

with the Laplace-operator ' Δ '.

- For \mathbf{m}_{\pm} :

$$\partial_{\theta_{\pm}} \pi = 0, \quad (42)$$

with the parametrization $\mathbf{m}_{\pm} = \cos \theta_{\pm} \mathbf{e}_1 + \sin \theta_{\pm} \mathbf{e}_2$.

Here, the last equation was not discussed in the 'weak form'-section, as the weak form is basically equivalent to the strong form, which will be exploited in the numerical solution algorithm presented below. Eq. (41)₂ physically means that the magnetostatic stray field is created by the mesoscopic magnetic 'charges' (in terms of $-\text{div}_2(\mathbf{M})$) located in the thin film. Further, the parametrization of the microscopic magnetization directions \mathbf{m}_{\pm} in terms of the angles $\underline{\theta} = (\theta_+, \theta_-)^T$ automatically satisfies the constraint $\|\mathbf{m}_{\pm}\| = 1$.

6. Numerical solution algorithm

6.1. Finite element discretization

The time-discrete problem outlined above is discretized by conventional finite elements with nodal variables $\{\gamma, d_{\text{eff}}, \xi, \varphi\}$. This standard procedure leads to a monolithic nonlinear equation system as discrete counterpart of the space-continuous Eqs. (38) and (39), which is linearized in order to be solved via Newton's method, as usual (see below). Eq. (42) is solved locally at the Gauss points of the thin film, also using Newton's method, involving the Newton step

$$\underline{\theta} \leftarrow \underline{\theta} - \underline{K}^{-1} \partial_{\underline{\theta}} \pi \quad (43)$$

with $\underline{K} = \partial_{\underline{\theta}}^2 \pi$.

The overall solution in terms of the nodal degrees of freedom is then obtained in the following standard fashion. Starting from the solution from the previous time step, the solution of the linearized global equations yields an increment of the nodal variables, which are then updated. Subsequently, the local problem related to θ_{\pm} is solved at all thin-film Gauss points via a local Newton procedure (see Eq. (43)). Based on this, the global equations are consistently linearized (see next section) in order to compute the next nodal variable update. This procedure is repeated until convergence of the global Newton procedure is reached.

For all initial solution guesses (required for the local and global Newton schemes), the respective converged values from the previous time step are used.

6.2. Consistent linearization

The overall variational global equation to be solved reads

$$\delta_{\underline{g}} \Pi := \delta_{\gamma} \Pi + \delta_{d_{\text{eff}}} \Pi + \delta_{\xi} \Pi + \delta_{\varphi} \Pi = h \int_A \partial_{\underline{x}} \pi \cdot \delta \underline{x} dA - \int_V \mu_0 \nabla \varphi \cdot \nabla \delta \varphi dV = 0 \quad (44)$$

with $\underline{x} = (\nabla \gamma, \nabla d_{\text{eff}}, \nabla \xi, \nabla \varphi, d_{\text{eff}}, \xi)$. The consistent linearization is given in terms of

$$\Delta(\delta_{\underline{g}} \Pi) = h \int_A \delta \underline{x} \cdot (\partial_{\underline{x}}^2 \pi - \partial_{\underline{x}} \partial_{\underline{\theta}} \pi \underline{K}^{-1} \partial_{\underline{\theta}} \pi) \Delta \underline{x} dA - \int_V \mu_0 \nabla \delta \varphi \cdot \nabla \Delta \varphi dV, \quad (45)$$

where \underline{K} is the tangent matrix of the local Newton scheme in the (locally) converged state. Eqs. (44) and (45) are discretized by standard finite elements, where linear tetrahedra/triangles are used in the example discussed below. Note that all matrices are symmetric due to the potential-structure of the continuum model. The model is implemented in the finite element software FEAP.⁴ The related element and integration point subroutines can be downloaded at [27].

Analogous algorithms are frequently applied for the mechanical simulation of materials with internal (local) variables (like plastic strains, see [26]) and require the aforementioned consistent linearization of the local algorithm in order to achieve quadratic convergence on the global level. Within the context of finite elements, this algorithm is usually preferred to other solution methods like the secant method, quasi-Newton methods or nonlinear conjugate gradients.

7. Exemplary simulation

While the primary goal of this work is the presentation of the mesoscopic continuum theory for stripe-shaped domains outlined above, a simple first simulation is performed in order to check if solutions can be obtained in general based on the derived equations and if these solutions are physically plausible. More extensive simulations, applications and validations will be left for future work.

⁴ FEAP: Finite Element Analysis Program, Robert Taylor, Berkeley.

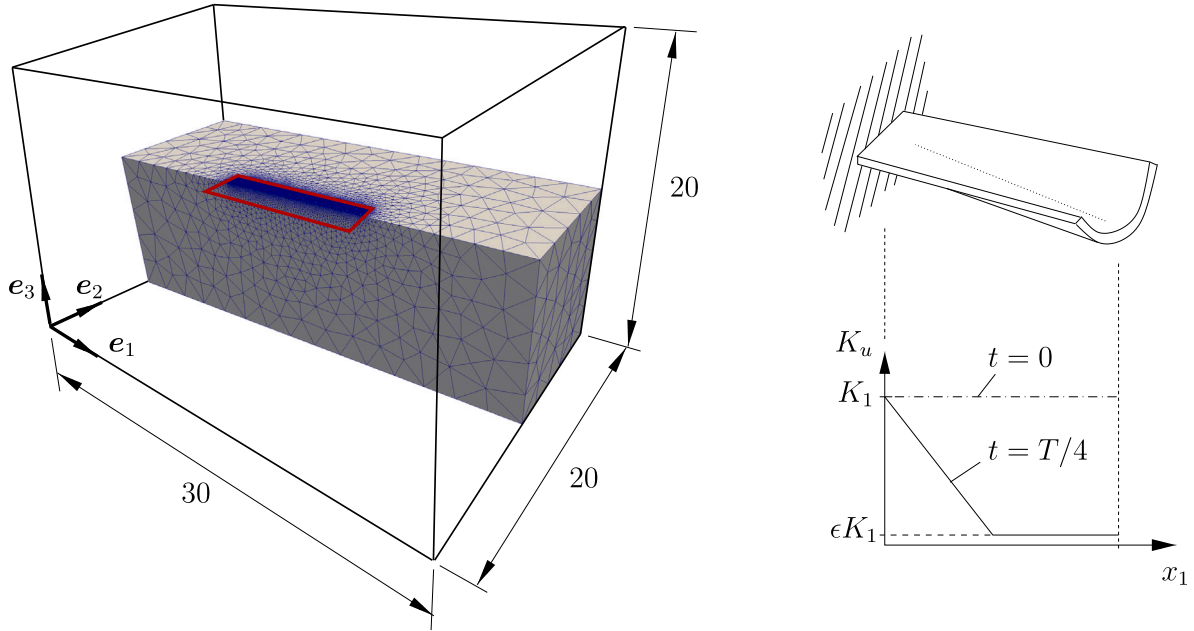


Fig. 4. Left: simulation set-up with thin film (red rectangle) in free-space box (dimensions in mm). Right, top: ‘U-Mode’ of a vibrating cantilever (deformation strongly exaggerated). Right, bottom: Effective anisotropy at times $t = 0$ and $t = T/4$.

7.1. General setting

For the simulation, a rectangular magnetostrictive thin film ($10 \times 2 \text{ mm}^2$, thickness $20 \mu\text{m}$ and modeled as a 2d-object), being embedded in the center of a free-space box (see Fig. 4, left) is considered. Only one quarter of the domain is meshed (by 8662 triangles and 44915 tetrahedra) for symmetry reasons. The aim is to simulate the application of an external field $H_{\text{ext}} = 8 \times 10^{-4} \text{ A}/\mu\text{m}$ in e_1 -direction, which is ramped up during the first 0.08s and is subsequently held constant. The easy axis is given by $e_a = e_2$. The thin film is considered as being deposited on top of a beam-shaped substrate (not part of the numerical model) with the same in-plane dimensions as the thin film and thickness in the order of 0.1 mm. The overall structure is assumed to be mechanically clamped on its left end (the face with normal $-e_1$). This set-up is motivated by a similar structure, which has been proposed by Hayes et al. [17] as basis for a highly sensitive magnetic field sensor. If the structure is stimulated to vibrate at a certain eigenfrequency, a specific eigenmode (called ‘U-mode’) is dominant, which is essentially characterized by a U-shaped deformation of the cross-sections (see Fig. 4, right). This mode leads to normal stresses in e_2 -direction in the thin film, which are alternately of compressive (see the figure) and tensile nature. These induce an alternating stress-induced anisotropy which superposes with the intrinsic anisotropy related to the easy axis. In practice, in particular the compressive stresses are of interest, since they induce an anisotropy opposed to the intrinsic anisotropy. As a result, the thin film becomes periodically magnetically softer, which can be exploited to detect weak magnetic fields in e_1 -direction.

7.2. Model parameters

In our model, mechanical influences are not captured and we therefore mimic the effect of the vibrating U-mode qualitatively by a time and space-dependent effective anisotropy constant K_u replacing K_1 in the model:

$$K_u = \begin{cases} K_1 - (1 - \epsilon)K_1 \frac{2(x_1 - L)}{L} \sin \Omega t, & x_1 \leq L/2 \\ (1 - \epsilon)K_1 \sin \Omega t, & x_1 > L/2 \end{cases} \quad (46)$$

Table 1

Model parameters.

μ_0 [N/A^2]	M^S [$\text{A}/\mu\text{m}$]	A [pJ/m]	K_1 [J/m^3]	k_ϕ [pJ/A^2]	η [$\text{J s}/\text{m}^3$]
$4\pi \times 10^{-7}$	1.5	15	300	0.1	0.1

with $\Omega = 2\pi/T = 20 \text{ s}^{-1}$, $\epsilon = 0.033$ and $L = 10 \text{ mm}$. For $t = T/4$ (i.e., after a quarter period) the anisotropy distribution is plotted in Fig. 4 (right, bottom).

The model parameters are summarized in Table 1. It is noted that Eq. (17) for k_ϕ yields values in the order of $1 \text{ pJ}/\text{A}^2$ or larger, which corresponds to a very high penalty parameter. For numerical robustness reasons, we choose a slightly smaller value. The viscosity parameter η is chosen sufficiently small, such that viscous effects are expected to be negligible. Further, the domain wall energy density σ_{DW} is computed according to the following Bloch wall formula

$$\sigma_{\text{DW}} = 4\sqrt{AK_1}. \quad (47)$$

It is noted that, compared to a micromagnetic model, no additional model parameters are needed.

7.3. Boundary conditions and initial solution guess

The domain walls are expected to enter and leave the thin film on its free end, while they are essentially immobile on the clamped side, where we consequently set the Dirichlet boundary condition $\gamma = 0$. Further, we set the closure domain phase field variable ξ equal to 1 on the long edges and set the magnetic potential ϕ to zero on the outer boundaries of the free space box. All other boundary conditions are treated as zero Neumann boundary conditions.

Based on simple energy considerations (comp. [4]), the domain wall distance can be estimated as

$$D = \sqrt{\frac{b \sigma_{\text{DW}}}{K_1}} = 2\sqrt{b\sqrt{\frac{A}{K_1}}}, \quad (48)$$

where b denotes the size of the magnetic film in e_2 -direction. This equation yields a value of $D = 42.3 \mu\text{m}$, which corresponds to approximately

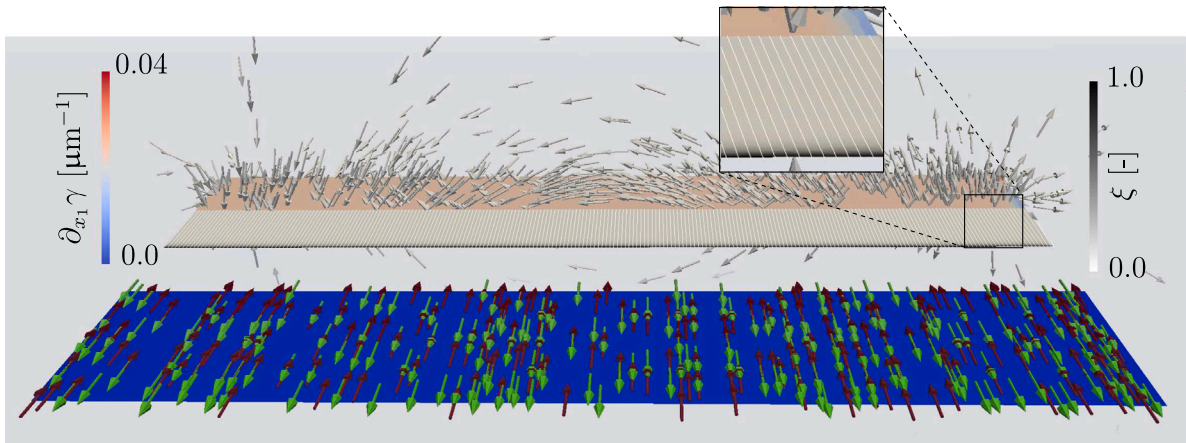


Fig. 5. Initial state.

236 domain walls in the initial state. This suggests for the initial guess⁵ of $\gamma(x, t = 0)$ as

$$\gamma = \hat{\gamma} \frac{x_1 - L}{L} \quad (49)$$

with $\hat{\gamma} = 236$. However, we choose a rather random value of $\hat{\gamma} = 41.8$ for two reasons. First, the model is supposed to find the ‘correct’ value of 236 by itself. Second, we want to illustrate the robustness of the solution algorithm in the sense that it is able to find the right solution even if the initial guess is quite far off from the actual solution. All other variables are initialized with the value 0 except for the microscopic magnetization directions, which are initialized by $\theta_+ = \pi/2$ and $\theta_- = 3\pi/2$. Based on this initialization, we let the algorithm find the initial conditions itself as follows:

- We do two Newton iterations at $t = 0$ as described in Section 6 where we iterate globally only in ξ with all other variables fixed.
- We do eight Newton iterations in γ .

Subsequently, the simulation starts as described in Section 6.

8. Results

8.1. Initial state

Fig. 5 shows the state after one time step at $t = 1 \mu\text{s}$, which essentially corresponds to the initial state. In order to illustrate the different solution fields, the magnetic layer is visualized twice (in the front and in the back). The green and dark red vectors in the front represent the microscopic magnetization directions m_{\pm} , which are initially aligned with the easy axis. The second thin film visualization in the back is divided along its long direction. The grayscale-field in the front half represents the closure domain phase field ξ . As expected, there is a thin closure domain region (black), which quickly fades out when moving away from the boundary. Further, the white lines are contour lines of the domain wall potential γ (see also the detail). It is recalled, that the contour lines are parallel to the domain walls and their distance is proportional to the domain wall distance. The maximum value of γ is found to be 234.6, which fits well with the aforementioned theoretical prediction of 236 expected domain walls. We therefore choose to plot 234 contour lines, i.e., each line may be interpreted roughly to represent one domain wall. It is emphasized that the continuum model is free of discrete domain walls and that the visualized lines are created merely by a postprocessing step. Note also, that the thickness of the closure domain layer at the boundary fits well to the domain wall distance, as intended.

Finally, the rearmost half of the thin film shows the field $\partial\gamma/\partial x_1 \approx \|\nabla\gamma\|$. This field can be interpreted as domain wall density, which is mostly homogeneous, as is also illustrated by the contour lines. The arrows in the free space indicate the direction (not magnitude) of the stray field. However, at this stage of the simulation, the stray field is still negligibly small.

8.2. State at maximum ‘bending’/minimum effective anisotropy

Next, we consider the situation of minimum effective anisotropy, which mimics the maximum bending according to the U-mode in Fig. 4 (right top). In this situation, the effective anisotropy is significantly decreased in the right part of the thin film (where $K_u = \epsilon K_1$), as prescribed by Eq. (46). This state is reached at $t = 0.5\pi/\Omega = T/4 \approx 0.078 \text{ s}$ (see the diagram in Fig. 4). It is noted that the external field in e_1 -direction reaches its maximum almost at the same time and is held constant afterwards.

The predicted fields are illustrated in Fig. 6. It is observed that the microscopic magnetization is no longer aligned with the easy axis but rotated due to the external field (see green and dark red vectors). The average magnetization in e_1 -direction, as expressed by

$$m_{\text{avg}} = \frac{1}{2}(m_+ + m_-) \cdot e_1, \quad (50)$$

is illustrated in rainbow colors. It reaches its maximum in the center and vanishes on the left and right ends (magnetization directions parallel to the edges), which corresponds to the boundary condition (41)₃. Along the length direction of the thin film, the non-vanishing divergence of the effective magnetization may be interpreted as distributed magnetic charge density. These charges act as source for the stray field (see Eq. (41)₂), the direction of which is visualized by arrows in the free space in the rearmost part of Fig. 6. Further, the colors (blue/red) in the free space give an impression of the magnetostatic potential.

As far as the domain wall density is concerned, a lower value is observed in the right part of the thin film. In other words, the domain wall distance is roughly doubled in this region. This is expected due to the lower value of K_u in this region. Theoretically, we expect a domain wall distance of approximately $D = 99.2 \mu\text{m}$, which is the value that is obtained if K_1 is replaced by $K_u = \epsilon K_1$ in Eq. (48).⁶ With a simulated domain wall density of $\partial_{x_1}\gamma \approx 0.01 \mu\text{m}^{-1}$ (see the right part of the rearmost field in Fig. 6), we find that the numerical value of $D \approx 100 \mu\text{m}$ is again very close to the analytical value.

⁶ Note that, despite the small value of $\epsilon = 0.033$ the domain wall distance does not increase as much as one might expect due to the double square root in Eq. (48), i.e., $\sqrt[4]{0.033} \approx 0.426$.

⁵ The global Newton scheme requires an initial solution guess.

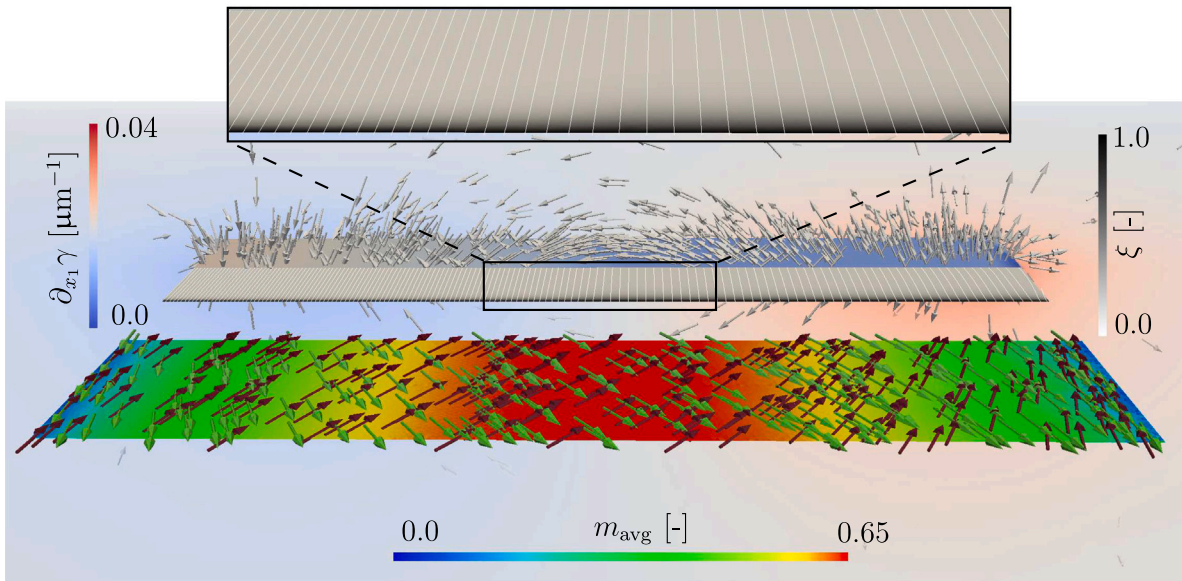


Fig. 6. State at $\sim K_{u,max}$ at $t = 0.078$ s (time step 63). The scale of the magnetic potential in the free space is $[-3.66, 3.8]$ A.

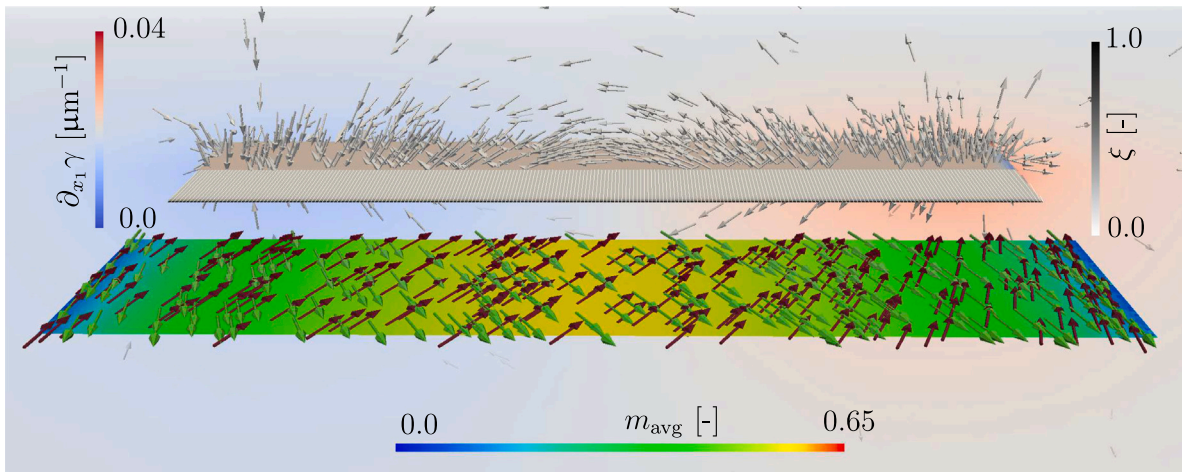


Fig. 7. State at $\sim K_{u,max}$ at $t = 0.157$ s (time step 126). The scale of the magnetic potential in the free space is again $[-3.66, 3.8]$ A.

Finally, the closure-domain phase field appears again as a thin boundary layer, but with the important difference that now this boundary layer exhibits a non-constant thickness (see detail of Fig. 6). Indeed, closure domains are expected to grow proportionally to the domain wall distance.

8.3. State at zero ‘bending’

Finally, we consider the state at $t = T/2 \approx 0.157$ s, which corresponds to the case, where $K_u = K_1$ is homogeneous in the whole thin film. The difference compared to the initial state in Section 8.1 is that the external field does not vanish, but takes the same value as in the previous Section 8.2. Accordingly, we expect a more or less homogeneous domain wall density being essentially equal to the one in the initial state, while the external field should rotate the magnetization directors out of the easy axis orientation.

Indeed, Fig. 7 shows that the effective magnetization decreases compared to the case with smaller effective anisotropy in Fig. 6. This effect leads to a smaller stray field and magnetostatic potential, being now visualized by slightly more pale blue and red colors in the free space region. As expected, the domain wall density essentially returns

Table 2

Exemplary residual evolution during global Newton iteration.

Step 63	Step 126
1.00000000E+00	1.00000000E+00
3.80455977E-02	2.49271470E-03
3.79634742E-04	9.58880044E-08
1.08398333E-07	
4.04406731E-12	

to its initial state and hardly any difference can be identified between the domain wall distances when comparing Figs. 5 and 7.

9. Short note on convergence

The L2-norm of the global relative residual is presented in Table 2. Due to the consistent linearization, the convergence can be considered quadratic. The illustrated convergence behavior is representative for the whole simulation. The total CPU-time until step 126 was $\sim 21,77$ min on an Intel(R) Core(TM) i7-8850H CPU @ 2.60 GHz with 32 GByte RAM.

10. Summary

Starting from a potential-based kinematical description of continuously distributed stripe-shaped domain walls, a mesoscopic potential has been derived through an averaging procedure. The mesoscopic theory is formulated in terms of a few fields with physically meaningful microscopic interpretation. Based on a phenomenological closure-domain extension, a constrained energy minimization principle (extended by ‘Gilbert’-damping) has been introduced and the related boundary value problem has been presented. A monolithic finite-element based numerical solution algorithm has been proposed with local treatment of the magnetization directors. Thanks to the consistent linearization, quadratic convergence could be obtained. A first simple examination of the theory has been undertaken by simulating a thin film with spatially and timely non-constant effective anisotropy. It has been found that the predicted results are reasonable and consistent with analytically computed values of the domain wall density.

Declaration of competing interest

The authors declare the following financial interests/personal relationships which may be considered as potential competing interests: Stephan Wulfighoff reports financial support was provided by Deutsche Forschungsgemeinschaft (DFG, German Research Foundation).

Christian Dorn reports financial support was provided by German Research Foundation.

Data availability

I have shared a link to the code within the manuscript.

Acknowledgments

This research was supported by the Deutsche Forschungsgemeinschaft (DFG, German Research Foundation) under project 286471992 (Collaborative Research Center 1261). Stephan Wulfighoff and Christian Dorn would like to gratefully acknowledge this financial support.

Appendix A. First derivatives of potential

In the following, we give the derivatives of the potential, which are required for the finite element implementation. In Section 3.6, the mesoscopic energy contributions are summarized. The related derivatives read

$$\partial_{\nabla\gamma}\pi = k_\varphi(M^S)^2 \left[2(\llbracket \mathbf{m} \rrbracket \cdot \mathbf{e}_{\text{DW}}^\perp) \llbracket \mathbf{m} \rrbracket + \left(\frac{1}{16} (\nabla d_{\text{eff}} \cdot \llbracket \mathbf{m} \rrbracket)^2 - (\llbracket \mathbf{m} \rrbracket \cdot \mathbf{e}_{\text{DW}}^\perp)^2 \right) \mathbf{e}_{\text{DW}}^\perp \right] \quad (\text{A.1})$$

$$+ \sigma_{\text{DW}} \mathbf{e}_{\text{DW}}^\perp + \Delta\psi_a \partial_{\nabla\gamma} \nu_+ - K_1 \frac{\|\nabla\xi\|^2}{\|\nabla\gamma\|^3} \mathbf{e}_{\text{DW}}^\perp - \mu_0 M^S \llbracket \mathbf{m} \rrbracket \cdot (\mathbf{H}_{\text{ext}} - \nabla\varphi) \partial_{\nabla\gamma} \nu_+ \quad (\text{A.2})$$

with $\Delta\psi_a = \psi_a(\mathbf{m}_+) - \psi_a(\mathbf{m}_-)$,

$$\partial_{\nabla d_{\text{eff}}}\pi = \frac{1}{8} k_\varphi (M^S)^2 (\nabla d_{\text{eff}} \cdot \llbracket \mathbf{m} \rrbracket) \|\nabla\gamma\| \llbracket \mathbf{m} \rrbracket, \quad (\text{A.3})$$

$$\partial_{d_{\text{eff}}}\pi = \Delta\psi_a \partial_{d_{\text{eff}}} \nu_+ - \mu_0 (\mathbf{H}_{\text{ext}} - \nabla\varphi) \cdot \partial_{d_{\text{eff}}} \mathbf{M}, \quad (\text{A.4})$$

$$\partial_{\nabla\xi}\pi = \frac{K_1}{\|\nabla\gamma\|^2} \nabla\xi, \quad \partial_\xi\pi = K_1 \xi, \quad (\text{A.5})$$

$$\partial_{\theta_\pm}\pi = \partial_{\mathbf{m}_\pm}\pi \cdot \mathbf{m}_\pm^\perp = \frac{\eta}{\Delta t} \Delta\theta_\pm + \left[\pm \partial_{\llbracket \mathbf{m} \rrbracket} \psi_\varphi + \partial_{\mathbf{m}_\pm} \psi_A - \mu_0 M^S \nu_\pm (\mathbf{H}_{\text{ext}} - \nabla\varphi) \right] \cdot \mathbf{m}_\pm^\perp \quad (\text{A.6})$$

with

$$\mathbf{m}_\pm^\perp = -\sin\theta_\pm \mathbf{e}_1 + \cos\theta_\pm \mathbf{e}_2 \quad (\text{A.7})$$

$$\partial_{\llbracket \mathbf{m} \rrbracket} \psi_\varphi = k_\varphi (M^S)^2 \|\nabla\gamma\| (2(\llbracket \mathbf{m} \rrbracket \cdot \mathbf{e}_{\text{DW}}^\perp) \mathbf{e}_{\text{DW}}^\perp + \frac{1}{8} (\nabla d_{\text{eff}} \cdot \llbracket \mathbf{m} \rrbracket) \nabla d_{\text{eff}}) \quad (\text{A.8})$$

$$\partial_{\mathbf{m}_\pm} \psi_A = -2\nu_\pm K_1 (\mathbf{m}_\pm \cdot \mathbf{e}_a) \mathbf{e}_a \quad (\text{A.9})$$

Appendix B. Second derivatives of potential

The second derivatives of the potential are summarized in the following.

$$\partial_{\nabla\gamma}^2 \pi = \left\{ \sigma_{\text{DW}} + k_\varphi (M^S)^2 \left[\frac{1}{16} (\nabla d_{\text{eff}} \cdot \llbracket \mathbf{m} \rrbracket)^2 - (\llbracket \mathbf{m} \rrbracket \cdot \mathbf{e}_{\text{DW}}^\perp)^2 + 2(\llbracket \mathbf{m} \rrbracket \cdot \mathbf{e}_{\text{DW}}) \right] \right\} \mathbf{Q}_{\text{DW}} \quad (\text{B.1})$$

$$+ \frac{1}{4} d_{\text{eff}} \Delta\psi_a - \frac{1}{4} d_{\text{eff}} \mu_0 M^S \llbracket \mathbf{m} \rrbracket \cdot (\mathbf{H}_{\text{ext}} - \nabla\varphi) \quad (\text{B.2})$$

$$+ \frac{K_1 \|\nabla\xi\|^2}{\|\nabla\gamma\|^4} (4\mathbf{e}_{\text{DW}}^\perp \otimes \mathbf{e}_{\text{DW}}^\perp - \mathbf{I}) \quad (\text{B.3})$$

with $\mathbf{Q}_{\text{DW}} = \partial_{\nabla\gamma} \mathbf{e}_{\text{DW}}^\perp = (\mathbf{I} - \mathbf{e}_{\text{DW}}^\perp \otimes \mathbf{e}_{\text{DW}}^\perp) / \|\nabla\gamma\|$.

$$\partial_{\nabla\gamma \nabla d_{\text{eff}}}\pi = \frac{1}{8} k_\varphi (M^S)^2 (\nabla d_{\text{eff}} \cdot \llbracket \mathbf{m} \rrbracket) \mathbf{e}_{\text{DW}}^\perp \otimes \llbracket \mathbf{m} \rrbracket \quad (\text{B.4})$$

$$\partial_{\nabla\gamma \nabla\xi}\pi = -2 \frac{K_1}{\|\nabla\gamma\|^3} \mathbf{e}_{\text{DW}}^\perp \otimes \nabla\xi \quad (\text{B.5})$$

$$\partial_{\nabla\gamma \nabla\varphi}\pi = \frac{\mu_0}{4} d_{\text{eff}} \mathbf{e}_{\text{DW}}^\perp \otimes (M^S \llbracket \mathbf{m} \rrbracket) \quad (\text{B.6})$$

$$\partial_{\nabla\gamma d_{\text{eff}}}\pi = \frac{1}{4} (\Delta\psi_a - \mu_0 M^S \llbracket \mathbf{m} \rrbracket \cdot (\mathbf{H}_{\text{ext}} - \nabla\varphi)) \mathbf{e}_{\text{DW}}^\perp \quad (\text{B.7})$$

$$\partial_{\nabla d_{\text{eff}}}^2 \pi = \frac{1}{8} k_\varphi (M^S)^2 \|\nabla\gamma\| \llbracket \mathbf{m} \rrbracket \otimes \llbracket \mathbf{m} \rrbracket \quad (\text{B.8})$$

$$\partial_{\nabla\xi}^2 \pi = \frac{K_1}{\|\nabla\gamma\|^2} \mathbf{I} \quad (\text{B.9})$$

$$\partial_{\nabla\varphi d_{\text{eff}}}\pi = \frac{1}{4} \mu_0 M^S \llbracket \mathbf{m} \rrbracket \|\nabla\gamma\| \quad (\text{B.10})$$

$$\partial_\xi^2 \pi = K_1 \quad (\text{B.11})$$

$$\partial_{\underline{\theta}} \pi = \begin{pmatrix} (\partial_{\nabla\gamma} \llbracket \mathbf{m} \rrbracket) \pi - 2\partial_{\nabla\gamma} \nu_+ K_1 (\mathbf{m}_+ \cdot \mathbf{e}_a) \otimes \mathbf{e}_a \\ -\mu_0 M^S \partial_{\nabla\gamma} \nu_+ \otimes (\mathbf{H}_{\text{ext}} - \nabla\varphi) \cdot \mathbf{m}_+^\perp \\ -(\partial_{\nabla\gamma} \llbracket \mathbf{m} \rrbracket) \pi - 2\partial_{\nabla\gamma} \nu_+ K_1 (\mathbf{m}_- \cdot \mathbf{e}_a) \otimes \mathbf{e}_a \\ -\mu_0 M^S \partial_{\nabla\gamma} \nu_+ \otimes (\mathbf{H}_{\text{ext}} - \nabla\varphi) \cdot \mathbf{m}_-^\perp \end{pmatrix}$$

with

$$\partial_{\llbracket \mathbf{m} \rrbracket \nabla\gamma}\pi = k_\varphi (M^S)^2 \left[2\mathbf{e}_{\text{DW}}^\perp \otimes \llbracket \mathbf{m} \rrbracket + 2(\llbracket \mathbf{m} \rrbracket \cdot \mathbf{e}_{\text{DW}}^\perp) \mathbf{e}_{\text{DW}} \otimes \mathbf{e}_{\text{DW}} + \frac{1}{8} (\nabla d_{\text{eff}} \cdot \llbracket \mathbf{m} \rrbracket) \nabla d_{\text{eff}} \otimes \mathbf{e}_{\text{DW}}^\perp \right] \quad (\text{B.12})$$

$$\partial_{\underline{\theta} \nabla d_{\text{eff}}}\pi = \begin{pmatrix} \partial_{\nabla d_{\text{eff}}} \llbracket \mathbf{m} \rrbracket \psi_\varphi \mathbf{m}_+^\perp \\ -\partial_{\nabla d_{\text{eff}}} \llbracket \mathbf{m} \rrbracket \psi_\varphi \mathbf{m}_-^\perp \end{pmatrix} \quad (\text{B.13})$$

$$\partial_{\llbracket \mathbf{m} \rrbracket \nabla d_{\text{eff}}}\psi_\varphi = \frac{k_\varphi}{8} (M^S)^2 \|\nabla\gamma\| (\nabla d_{\text{eff}} \otimes \llbracket \mathbf{m} \rrbracket + (\nabla d_{\text{eff}} \cdot \llbracket \mathbf{m} \rrbracket) \mathbf{I}) \quad (\text{B.14})$$

$$\partial_{\underline{\theta} \nabla\varphi}\pi = \begin{pmatrix} \mu_0 M^S \nu_+ \mathbf{m}_+^\perp \\ \mu_0 M^S \nu_- \mathbf{m}_-^\perp \end{pmatrix} \quad (\text{B.15})$$

$$\partial_{\underline{\theta} d_{\text{eff}}}\pi = \begin{pmatrix} -2K_1 (\mathbf{m}_+ \cdot \mathbf{e}_a) (\mathbf{m}_+^\perp \cdot \mathbf{e}_a) - \mu_0 M^S (\mathbf{H}_{\text{ext}} - \nabla\varphi) \cdot \mathbf{m}_+^\perp \\ 2K_1 (\mathbf{m}_- \cdot \mathbf{e}_a) (\mathbf{m}_-^\perp \cdot \mathbf{e}_a) + \mu_0 M^S (\mathbf{H}_{\text{ext}} - \nabla\varphi) \cdot \mathbf{m}_-^\perp \end{pmatrix}$$

Components of \underline{K} :

$$\partial_{\theta_\pm}^2 \pi = (\partial_{\llbracket \mathbf{m} \rrbracket}^2 \psi_\varphi + \partial_{\mathbf{m}_\pm}^2 \psi_A) : \mathbf{m}_\pm^\perp \otimes \mathbf{m}_\pm^\perp - \partial_{\mathbf{m}_\pm} \pi \cdot \mathbf{m}_\pm + \frac{\eta}{\Delta t} \quad (\text{B.16})$$

$$= 2k_\varphi (M^S)^2 \|\nabla\gamma\| \left((\mathbf{e}_{\text{DW}}^\perp \cdot \mathbf{m}_\pm^\perp)^2 + \frac{1}{16} (\nabla d_{\text{eff}} \cdot \mathbf{m}_\pm^\perp)^2 \right) - \partial_{\mathbf{m}_\pm} \pi \cdot \mathbf{m}_\pm \quad (\text{B.17})$$

$$- 2\nu_\pm K_1 (\mathbf{e}_a \cdot \mathbf{m}_\pm^\perp)^2 + \frac{\eta}{\Delta t}$$

$$\partial_{\theta_\pm \theta_\mp} \pi = -2k_\varphi (M^S)^2 \|\nabla\gamma\| \left((\mathbf{e}_{\text{DW}}^\perp \cdot \mathbf{m}_+^\perp) (\mathbf{e}_{\text{DW}}^\perp \cdot \mathbf{m}_-^\perp) + \frac{1}{16} (\nabla d_{\text{eff}} \cdot \mathbf{m}_+^\perp) (\nabla d_{\text{eff}} \cdot \mathbf{m}_-^\perp) \right) \quad (\text{B.17})$$

Appendix C. Estimation of k_φ

We consider a rectangle (representing a domain-wall) being occupied by a surface charge

$$\sigma = -\mu_0 M^S \llbracket \mathbf{m} \rrbracket \cdot \mathbf{e}_x \quad (\text{C.1})$$

with height h in $e_{3/z}$ -direction and infinite extension in e_y -direction in the thin-film plane. The e_x -direction coincides with the rectangle normal. The aim is to estimate the stray field energy of this surface charge. With the well-known potential of an infinite line-charge, we obtain for the surface charge

$$\varphi(\mathbf{x}) = -\frac{1}{2\pi\mu_0} \int_{h/2}^{h/2} \frac{\sigma}{2} \ln\left(\frac{\|\mathbf{x} - \mathbf{x}'\|^2}{r_0^2}\right) dz', \quad (\text{C.2})$$

where, with a little abuse of notation, we use the same symbol φ as for the mesoscopic stray field. The parameter r_0 corresponds to an integration constant.

A lengthy derivation yields

$$\begin{aligned} \varphi = & -\frac{\sigma}{4\pi\mu_0} \left(\frac{h}{2} - z\right) \ln\left(\frac{x^2 + (z - h/2)^2}{r_0^2}\right) \\ & - \frac{\sigma}{4\pi\mu_0} \left(\frac{h}{2} + z\right) \ln\left(\frac{x^2 + (z + h/2)^2}{r_0^2}\right) \\ & + \frac{\sigma h}{2\pi\mu_0} + \dots, \end{aligned} \quad (\text{C.3})$$

where the dots represent terms, which are not needed as they vanish for $x \rightarrow 0$, i.e., within the aforementioned surface charge.

We assume that expression (C.3) represents a reasonable approximation of the stray field within a cylinder with axis given by the e_y -direction, radius $R \gg h$ and cross section A_R . We do not consider the limit $R \rightarrow \infty$ as the surface charge is actually not infinitely extended in e_y -direction. Neglecting stray field interactions, the energy (in the cylinder) per unit domain wall length reads

$$\frac{\Delta E}{\Delta L} = \frac{1}{2}\mu_0 \int_{A_R} \|\nabla\varphi\|^2 dA = \frac{1}{2}\mu_0 \int_{\partial A_R} \varphi \mathbf{n} \cdot \nabla\varphi dS + \frac{1}{2} \int_{-h/2}^{h/2} \sigma\varphi dz. \quad (\text{C.4})$$

On ∂A_R , φ can safely be approximated by the potential of a line charge σh and one finds

$$\frac{1}{2}\mu_0 \int_{\partial A_R} \varphi \mathbf{n} \cdot \nabla\varphi dS = \frac{\sigma^2 h^2}{4\pi\mu_0} \left(\ln\left(\frac{R}{r_0}\right) - 1\right) \quad (\text{C.5})$$

Evaluating the last integral in Eq. (C.4) and requiring energy equality with expression (16), i.e.,

$$E_\varphi = k_\varphi \int_{\Delta A_{\text{DW}}} (M^S \|\mathbf{m}\| \cdot \mathbf{n})^2 dA = \frac{k_\varphi}{\mu_0^2} \sigma^2 \Delta A_{\text{DW}} \quad (\text{C.6})$$

$$\stackrel{!}{=} \frac{\Delta E}{\Delta L h} \Delta A_{\text{DW}} = \frac{\sigma^2 h^2}{4\pi\mu_0} \underbrace{\left(\ln\left(\frac{R}{h}\right) + \frac{1}{2}\right)}_{=: D} \frac{\Delta A_{\text{DW}}}{h}, \quad (\text{C.7})$$

we finally obtain

$$k_\varphi = D \frac{\mu_0 h}{4\pi}. \quad (\text{C.8})$$

For reasonable choices of R , the parameter D can be estimated to be in the order 1..10. Note that the integration constant r_0 cancels out in the final result and its value can therefore be chosen arbitrarily.

Appendix D. Rate potential

The time continuous counterpart of Eq. (36) reads

$$\Pi_I = h \int_A \left(\frac{\partial\psi}{\partial\mathbf{m}_+} \cdot \dot{\mathbf{m}}_+ + \frac{\partial\psi}{\partial\mathbf{m}_-} \cdot \dot{\mathbf{m}}_- + \phi(\dot{\mathbf{m}}_+, \dot{\mathbf{m}}_-) - \mu_0(\mathbf{H}_{\text{ext}} - \nabla\varphi) \cdot \dot{\mathbf{M}} \right) dA. \quad (\text{D.1})$$

with

$$\phi(\dot{\mathbf{m}}_+, \dot{\mathbf{m}}_-) = \lim_{\Delta t \rightarrow 0} \frac{1}{\Delta t} \phi_\Delta(\dot{\mathbf{m}}_+, \dot{\mathbf{m}}_-) \quad (\text{D.2})$$

with $\phi = \frac{\eta}{2}(\dot{\theta}_+^2 + \dot{\theta}_-^2)$.

References

- [1] W. Rave, R. Schäfer, A. Hubert, Quantitative observation of magnetic domains with the magneto-optical Kerr effect, *J. Magn. Magn. Mater.* 65 (1) (1987) 7–14.
- [2] J. McCord, Progress in magnetic domain observation by advanced magneto-optical microscopy, *J. Phys. D: Appl. Phys.* 48 (33) (2015) 333001.
- [3] W.F. Brown, *Magnetoelastic Interactions*, Vol. 9, Springer, 1966.
- [4] H. Kronmüller, M. Fähnle, *Micromagnetism and the Microstructure of Ferromagnetic Solids*, Cambridge University Press, 2003.
- [5] A. Hubert, R. Schäfer, *Magnetic Domains: The Analysis of Magnetic Microstructures*, Springer Science & Business Media, 2008.
- [6] J.M. Coey, *Magnetism and Magnetic Materials*, Cambridge University Press, 2010.
- [7] N.O. Urs, I. Teliban, A. Piorra, R. Knöchel, E. Quandt, J. McCord, Origin of hysteretic magnetoelastic behavior in magnetoelastic 2-2 composites, *Appl. Phys. Lett.* 105 (20) (2014) 202406.
- [8] C. Dorn, M. Hörsting, J. Schmalz, S. Wulfinhoff, M. Jovičević-Klug, N.O. Urs, E. Spetzler, J. McCord, Self-emergence of undulating magnetic domains in magnetostrictive films, 2023, (in preparation).
- [9] L. Landau, E. Lifshitz, On the theory of the dispersion of magnetic permeability in ferromagnetic bodies, *Phys. Z. Sowjetunion* 8 (1935) 153–169.
- [10] T.L. Gilbert, A phenomenological theory of damping in ferromagnetic materials, *IEEE Trans. Magn.* 40 (6) (2004) 3443–3449.
- [11] C. Miehe, G. Ethiraj, A geometrically consistent incremental variational formulation for phase field models in micromagnetics, *Comput. Methods Appl. Mech. Engrg.* 245 (2012) 331–347.
- [12] M. Yi, B.-X. Xu, A constraint-free phase field model for ferromagnetic domain evolution, *Proc. R. Soc. Lond. Ser. A Math. Phys. Eng. Sci.* 470 (2171) (2014) 20140517.
- [13] M.-A. Keip, A. Sridhar, A variationally consistent phase-field approach for micro-magnetic domain evolution at finite deformations, *J. Mech. Phys. Solids* 125 (2019) 805–824.
- [14] A. Sridhar, M.-A. Keip, C. Miehe, Homogenization in micro-magneto-mechanics, *Comput. Mech.* 58 (2016) 151–169.
- [15] C. Dorn, S. Wulfinhoff, Computing magnetic noise with micro-magneto-mechanical simulations, *IEEE Trans. Magn.* (2022).
- [16] A. Kittmann, P. Durdaut, S. Zabel, J. Reermann, J. Schmalz, B. Spetzler, D. Meyners, N.X. Sun, J. McCord, M. Gerken, et al., Wide band low noise love wave magnetic field sensor system, *Sci. Rep.* 8 (1) (2018) 278.
- [17] P. Hayes, M. Jovičević Klug, S. Toxvæ rd, P. Durdaut, V. Schell, A. Teplyuk, D. Burdin, A. Winkler, R. Weser, Y. Fetisov, et al., Converse magnetoelectric composite resonator for sensing small magnetic fields, *Sci. Rep.* 9 (1) (2019) 16355.
- [18] J.F. Nye, Some geometrical relations in dislocated crystals, *Acta Metall.* 1 (2) (1953) 153–162.
- [19] E. Kröner, *Kontinuumstheorie der Versetzungen und Eigenspannungen*, Vol. 5, Springer, 1958.
- [20] M. Ashby, The deformation of plastically non-homogeneous materials, *Philos. Mag.: J. Theor. Exp. Appl. Phys.* 21 (170) (1970) 399–424.
- [21] I. Steinbach, Phase-field models in materials science, *Model. Simul. Mater. Sci. Eng.* 17 (7) (2009) 073001.
- [22] C. Miehe, F. Welschinger, M. Hofacker, Thermodynamically consistent phase-field models of fracture: Variational principles and multi-field FE implementations, *Internat. J. Numer. Methods Engrg.* 83 (10) (2010) 1273–1311.
- [23] C. Miehe, A multi-field incremental variational framework for gradient-extended standard dissipative solids, *J. Mech. Phys. Solids* 59 (4) (2011) 898–923.
- [24] M. Ortiz, L. Stainier, The variational formulation of viscoplastic constitutive updates, *Comput. Methods Appl. Mech. Engrg.* 171 (3–4) (1999) 419–444.
- [25] C. Miehe, J. Schotte, M. Lambrecht, Homogenization of inelastic solid materials at finite strains based on incremental minimization principles. Application to the texture analysis of polycrystals, *J. Mech. Phys. Solids* 50 (10) (2002) 2123–2167.
- [26] J.C. Simo, R.L. Taylor, Consistent tangent operators for rate-independent elastoplasticity, *Comput. Methods Appl. Mech. Engrg.* 48 (1) (1985) 101–118.
- [27] S. Wulfinhoff, Code used for “A continuum theory for stripe-shaped magnetic domains in thin films”, 2023, URL <https://doi.org/10.57892/100-7>.